Supplementary material for: High-resolution direct simulation of deep water breaking waves: transition to turbulence, bubbles and droplets production

W. MOSTERT[1,2], S. POPINET[3] and L. DEIKE[1,4]

[1]Mechanical & Aerospace Engineering, Princeton University, Princeton NJ 08544, USA
[2]Department of Mechanical and Aerospace Engineering, Missouri University of Science and Technology, Rolla MO 65401, USA
[3]Institut Jean Le Rond d'Alembert, CNRS UMR 7190, Sorbonne Université, Paris, France
[4]High Meadows Environmental Institute, Princeton University, Princeton NJ 08544, USA

(Received xx; revised xx; accepted xx)

The Supplementary Materials presents detailed convergence data and discussion regarding the energy dissipation (in 2D and 3D), as well as the bubble and droplet size distributions.

1. Grid structure and mesh refinement scheme

We use the adaptive mesh refinement (AMR) method implemented in the Basilisk library to solve the two-phase incompressible Navier-Stokes equations with surface tension, in 2D and 3D. The structure of the code is described in Popinet (2003, 2009, 2018); Fuster & Popinet (2018); van Hooft *et al.* (2018).

The numerical mesh is adaptively refined in order to reduce computational cost. To facilitate such a scheme within a Cartesian grid structure, a tree-based grid is used, which allows non-uniform resolution across the computational domain. In a given region of the grid, the numerical grid comprises multiple coexisting, hierarchical resolution *levels*, ranging from zero to a local maximum resolution, and where the grid size between any two levels varies by a factor of two. The global maximum resolution level L is specified by the user. The grid cells at a given location and resolution level are termed the *children* of those at the next lower level, and the *parents* of those at the next higher level. Cells that do not have children are termed *leaf* cells. Spatially neighbouring leaf cells may differ by up to one level.

Cartesian stencils are easily defined across the entire spatial domain by the employment of *ghost* cells. If a stencil is required at a resolution boundary, i.e. where neighbouring leaf cells are at different levels, the coarse-side leaf cells are called *halo* cells and given children cells (the ghosts) which are therefore at the same resolution level as the leaf cells on the fine side of the boundary. The regular Cartesian stencil then applies naturally at the boundary. The flow variables of interest in the ghost cells are defined by using information in the halo cells, e.g. by interpolation.

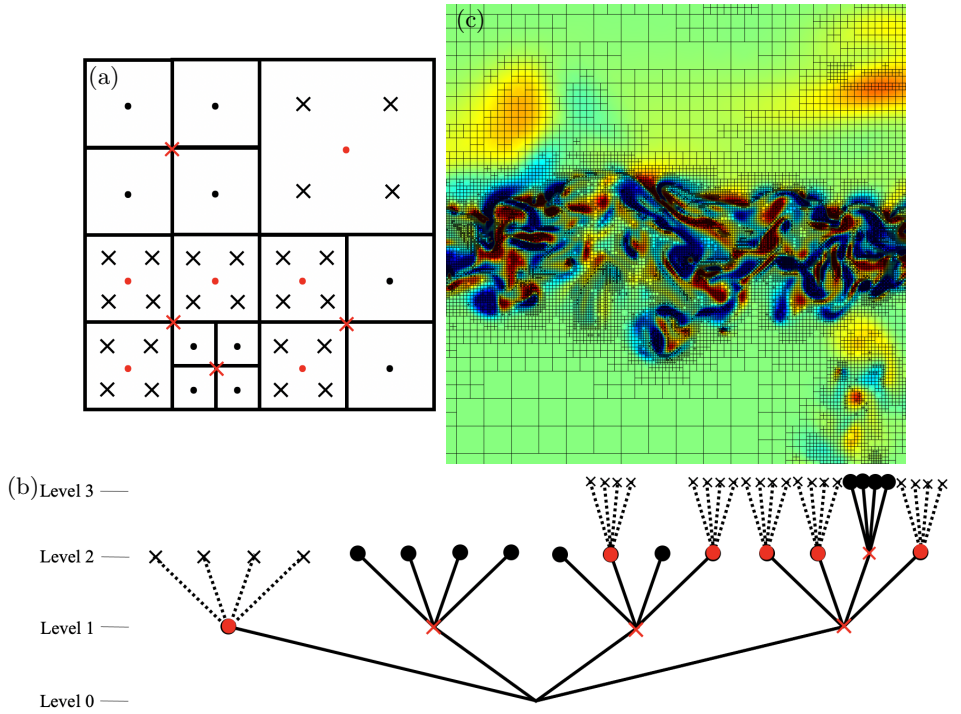

FIGURE 1. (a) Schematic illustration of the adaptive mesh refinement (AMR) grid structure. Leaf cell centres are indicated by dots; halo (leaf) cell centres are indicated by red dots. Ghost cell centres are indicated by crosses. At resolution boundaries, regular cells and ghost cells of the same colour together define regular Cartesian stencils for numerical operations. For example, at the boundary to the finest resolution zone, black points and crosses define a fine Cartesian stencil, while the red points and crosses define a coarse Cartesian stencil; both such stencils are regularly spaced. See text for complete description. (b) Tree structure of the grid corresponding to that of (a). (a) and (b) are adapted from Figure 2 of van Hooft *et al.* (2018). (c) Cross section of a breaking wave simulation from this study, $\mathrm{Bo} = 1000, \mathrm{Re} = 10^4, L = 11$ at $t/T = 1.8$, showing vorticity (coloured contour) with the mesh overlaid.

The refinement and coarsening scheme itself is based on a wavelet-estimation algorithm. Whether a grid is locally refined or coarsened depends on a choice of the flow variables, on the maximum tolerated errors for these variables, and on the maximum refinement level L of the numerical mesh. Errors in a given flow variable within a given region are estimated as follows. The finest mesh representation of the variable is locally downsampled into a coarser resolution. This new coarse representation is then re-interpolated onto the same grid points as the original fine representation. The absolute difference between the original and re-interpolated samples at the sampling points is an estimate for the local discretization error of the fine representation. The grid will then refine or coarsen based on whether this estimate is greater or smaller than the tolerance criterion. The error associated with this refinement-coarsening scheme is essentially an interpolation error, in that it does not reflect the error of the underlying numerical scheme, and is typically proportional to the norm of the second derivative of the relevant flow variables, and thus second-order. In the simulations in this study,

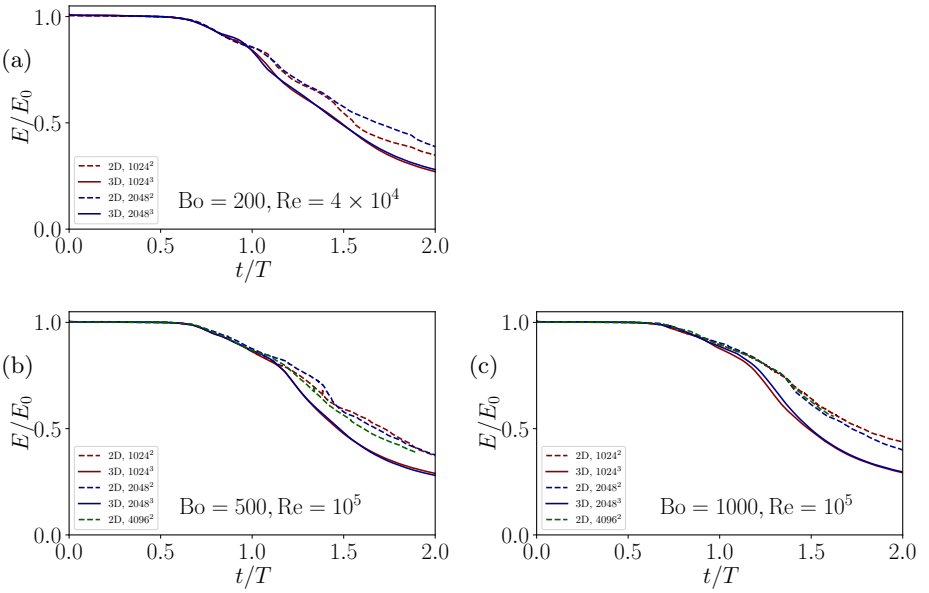

FIGURE 2. Time evolution of budgets of the mechanical energy $E = E_P + E_K$ for 2D (dashed) and 3D (solid), at resolution levels $L = 10$ (red), $L = 11$ (blue), and where applicable $L = 12$ (green) for cases (a) $\mathrm{Bo} = 200, \mathrm{Re} = 4 \times 10^4$, (b) $\mathrm{Bo} = 500, \mathrm{Re} = 10^5$, (c) $\mathrm{Bo} = 1000, \mathrm{Re} = 10^5$.

the flow variables of interest are the VOF and velocity fields. For an extended description of the AMR scheme, see van Hooft *et al.* (2018).

2. Numerical convergence

2.1. *Energetics*

In this section we discuss the numerical convergence of the results with respect to energetics. First, we consider the time evolution of the budget of the wave mechanical energy $E = E_P + E_K$, where E_P, E_K are the gravitational potential and kinetic energies integrated over the liquid phase. Figure 2 shows the budgets of four cases with various Bond and Reynolds numbers, including comparisons of both 2D and 3D simulations, for maximum resolution levels $L = 10, 11$, corresponding to effective cell counts of $(2^L)^d$, where d is the dimension of simulation. For the cases $\mathrm{Re} = 10^5$, we also plot $L = 12$ results. In each case, all results are well-converged at early times after breaking, up to $t \sim 1.1T$. The 3D results are very close to each other between the two numerical resolution.

Next, figure 3 shows convergence data for the instantaneous dissipation rate, ϵ. In each graph is plotted the 2D and 3D dissipation rates, $\epsilon_{2D}, \epsilon_{3D}$ at the same resolution levels as in figure 2. For $\mathrm{Bo} = 200, \mathrm{Re} = 4 \times 10^4$ (3a), dissipation rates are similar in both shape and magnitude for both 2D and 3D cases, with slight differences in precise timing of the peak shortly after $t = T$. For the cases $\mathrm{Re} = 10^5$ (3b,c), for $L = 10, 11$, the data agree in general shape. A $L = 12$ case is prohibitively expensive to produce in 3D at the moment. Comparing $L = 10, 11, 12$ in the 2D results of figure 3b, we see that the agreement between $L =$

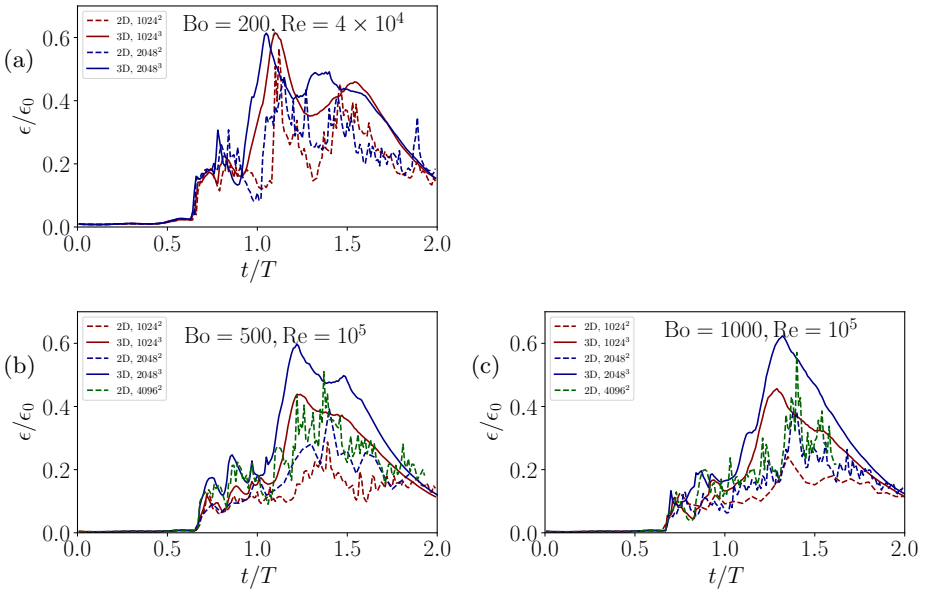

FIGURE 3. Time evolution of budgets of the dissipation rate ϵ for 2D (dashed) and 3D (solid), at resolution levels $L = 10$ (red), $L = 11$ (blue), and where applicable $L = 12$ (green) for cases (a) $\mathrm{Bo} = 200, \mathrm{Re} = 4 \times 10^4$, (b) $\mathrm{Bo} = 500, \mathrm{Re} = 10^5$, (c) $\mathrm{Bo} = 1000, \mathrm{Re} = 10^5$.

$11, 12$ is better than between $L = 10, 11$. In figure 3c, the $L = 11, 12$ results almost coincide.

As well as using direct comparisons of numerical data, we may also estimate the relevant length scales in the flow relative to the smallest mesh size in the simulations. First, the Batchelor's estimate for the viscous sublayer underneath the prebroken wave has been used in other investigations (see for example Deike *et al.* (2015); De Vita *et al.* (2018)), where $\delta \sim \lambda_0/\sqrt{Re}$. In these investigations, a resolution of at least four cells within the boundary layer, i.e. $\delta/\Delta x \gtrapprox 4$, was found to be sufficient for numerical convergence. Table 1 shows estimates of δ/λ_0 (second column) and number of grid points per boundary layer thickness (seventh column) for various Re, L. This suggests that $L = 10$ is sufficient for the cases $\mathrm{Re} = 4 \times 10^4$, and likewise $L = 11$ is sufficient for $\mathrm{Re} = 10^5$, consistent with the comparisons above. $L = 11$ also appears sufficiently large for $\mathrm{Re} = 2 \times 10^5$, although direct numerical comparisons are not available for these cases.

Another estimate is provided by the Kolmogorov scale, as is often done in traditional DNS of turbulence (Pope 2000; Dodd *et al.* 2021). Here, the Kolmogorov length scale $\eta = (\nu_w^3/\varepsilon)^{1/4}$ is compared with a maximum resolvable wavenumber $k_{max} = \pi 2^L/\lambda_0 = \pi/\Delta x$. In order to make this estimate for a given case, we take the maximum value of ε, to provide a conservatively small estimate for η. The resulting estimates for η and $k_{max}\eta$ are shown in the third and eighth columns of table 1. This estimate suggests that $L = 10$ is sufficient for $\mathrm{Re} = 4 \times 10^4$ and $L = 11$ is sufficient for $\mathrm{Re} = 10^5$, consistent with the above comparisons.

All estimates of numerical convergence therefore suggest that $L = 11$ provides

Re	δ/λ_0	η/λ_0	L	$\Delta x/\lambda_0$	$k_{max}\lambda_0$	$\delta/\Delta x$	$k_{max}\eta$
4×10^4	5×10^{-3}	5.28×10^{-4}	10	9.77×10^{-4}	3217	5.12	1.70
			11	4.88×10^{-4}	6434	10.2	3.39
10^5	3.16×10^{-3}	2.74×10^{-4}	10	9.77×10^{-4}	3217	3.24	0.88
			11	4.88×10^{-4}	6434	6.5	1.76
2×10^5	2.24×10^{-3}	1.63×10^{-4}	10	9.77×10^{-4}	3217	2.29	0.52
			11	4.88×10^{-4}	6434	4.58	1.05

TABLE 1. Numerical parameters and criteria for resolving energetics in the evolving flow. The column labels are as follows: Re - Reynolds number; δ/λ_0 - ratio of viscous boundary layer thickness, defined here as $\delta = \lambda_0/\sqrt{\mathrm{Re}}$, to wavelength; η/λ_0 - ratio of estimated Kolmogorov length scale to wavelength; L - maximum level of grid refinement; $\Delta x/\lambda_0$ - ratio of grid size to wavelength; k_{max}/λ_0 - wavelength-normalized maximum resolvable wavenumber; $\delta/\Delta x$ - ratio of viscous boundary layer thickness to grid size; $k_{max}\eta$ - criterion for sufficient resolution of Kolmogorov scales.

sufficient resolution for $\mathrm{Re} = 4\times10^4, 10^5$. The status of $\mathrm{Re} = 2\times10^5$ is uncertain because direct comparison data is not available for this Reynolds number.

2.2. *Bubble statistics*

Figure 4 shows different contours showing bubble size distribution(vertical axis) over time (horizontal axis), for the three main cases presented in the study. The horizontal axis is shifted so that the instant of jet impact is at zero. By comparing the first column of figures with the second, the following features become evident: (i) All cases predict a large "bubble" (i.e. the main cavity) which is produced on impact and which persists for approximately the same amount of time; (ii) The breakup of this large cavity is associated with the production of a limited number of large bubbles, and that the particular set of large bubbles produced in this way varies by resolution for all cases; (iii) All cases show an initially comparatively small amount of small bubbles produced on impact, followed by a much broader and populous range of bubbles produced by not later than $(t-t_{im})/T \simeq 0.2$, but the evolution is not identical across different resolutions or cases. Thus the various bubble populations share the same qualitative features, but are not pointwise-converged. This is expected because as a turbulent multiphase flow, we do not expect two realizations of the same nominal initial condition to be identical. To establish such convergence an ensemble-average would be needed, which is not feasible at the present resolutions, given the computation cost.

Figure 5 shows the same cases as figure 4 for time windows of width $\Delta = 0.4$ centred at $(t-t_{im})/T = 0.2, 0.6, 1$. In this comparison, data is well-converged at small (abundant) bubble sizes, and less so at large (scarce) bubble sizes. As the Bond number increases, the number of total bubbles supported by the breaker increases and convergence is better established. Finally, figure 6 shows numerical convergence for bubble size distributions in the cases $Bo = 200, Re = 4\times10^4$, $Bo = 500, Re = 4\times10^4$, $Bo = 500, Re = 10^5$, $Bo = 1000, Re = 10^5$, averaged

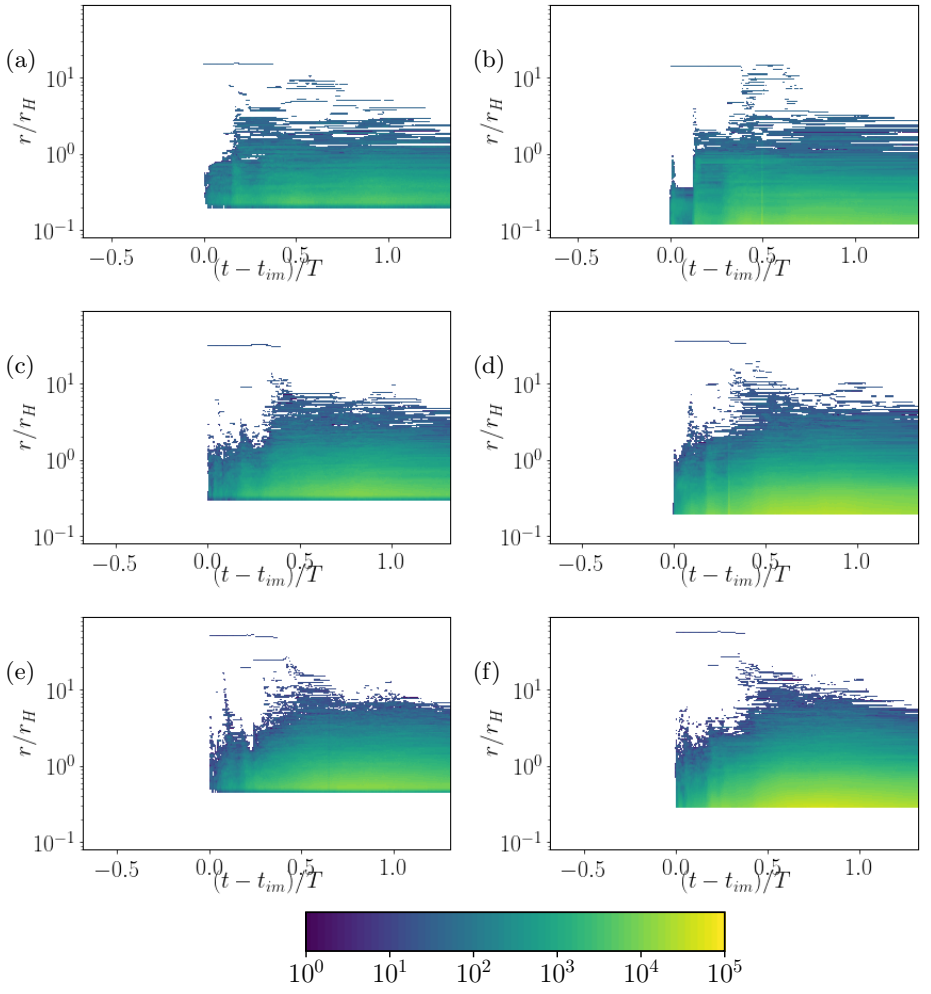

FIGURE 4. Bubble contour plots for different Bo, Re, and resolution. (a,b) $Bo = 200, Re = 4 \times 10^4$; (c,d) $Bo = 500, Re = 10^5$, (e,f) $Bo = 1000, Re = 10^5$. Resolutions are: (a,c,e) $L = 10$; (b,d,f) $L = 11$.

over the times $(t - t_{im})/T \in [0.4, 1.2]$, for the resolution parameters $L = 10, 11$, corresponding with minimum grid sizes of $\Delta x = 1/(2^L)$. All cases appear well converged.

2.3. *Droplet statistics*

As for the bubble data, figure 7 shows different contours showing droplet size distribution (vertical axis) over time (horizontal axis), for the three main cases presented in the study. The data for $\mathrm{Bo} = 200, \mathrm{Re} = 4 \times 10^4$ (7a,b) is not comparable at levels $L = 10, 11$ and are not grid converged. The data for $\mathrm{Bo} = 500, 1000$ (7c-f) do show more qualitative similarities, but, like the bubble data, are not pointwise-converged.

Figure 8 shows the same cases as figure 7 for the same time windows shown in figure 5. Again, the $\mathrm{Bo} = 200$ (8a) data is not converged at any time, nor is $\mathrm{Bo} = 500, \mathrm{Re} = 4 \times 10^4$ (8b), but the latest time window of $\mathrm{Bo} = 500, \mathrm{Re} = 10^5$

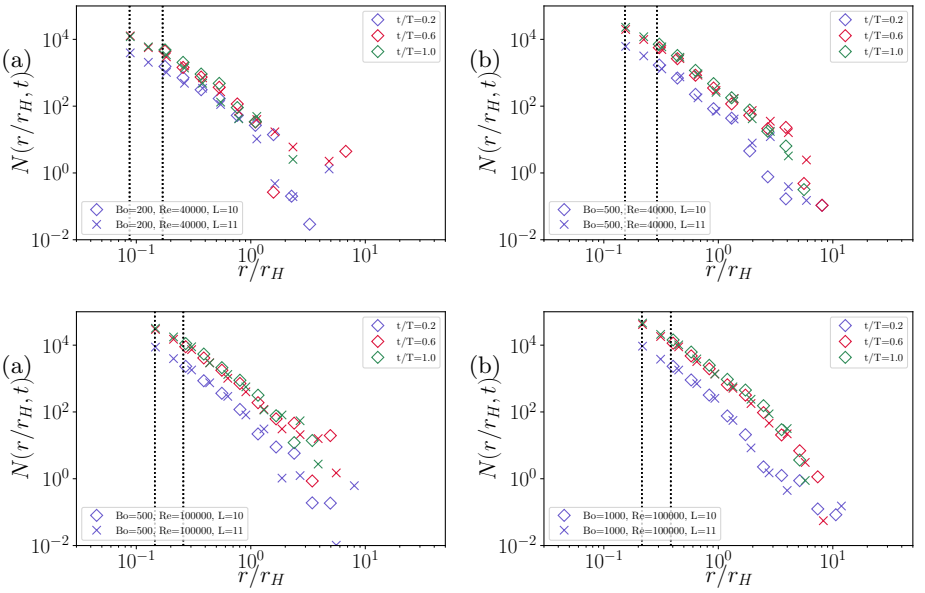

FIGURE 5. Numerical convergence of different time-averaging windows of bubble size distributions. Time-averaging windows are of width $\Delta t/T = 0.4$, and centered at $t/T = 0.2, 0.6, 1$, for cases (a) Bo $= 200, \mathrm{Re} = 4 \times 10^4$, (b) Bo $= 500, \mathrm{Re} = 4 \times 10^4$, (c) Bo $= 500, \mathrm{Re} = 10^5$, (d) Bo $= 1000, \mathrm{Re} = 10^5$.

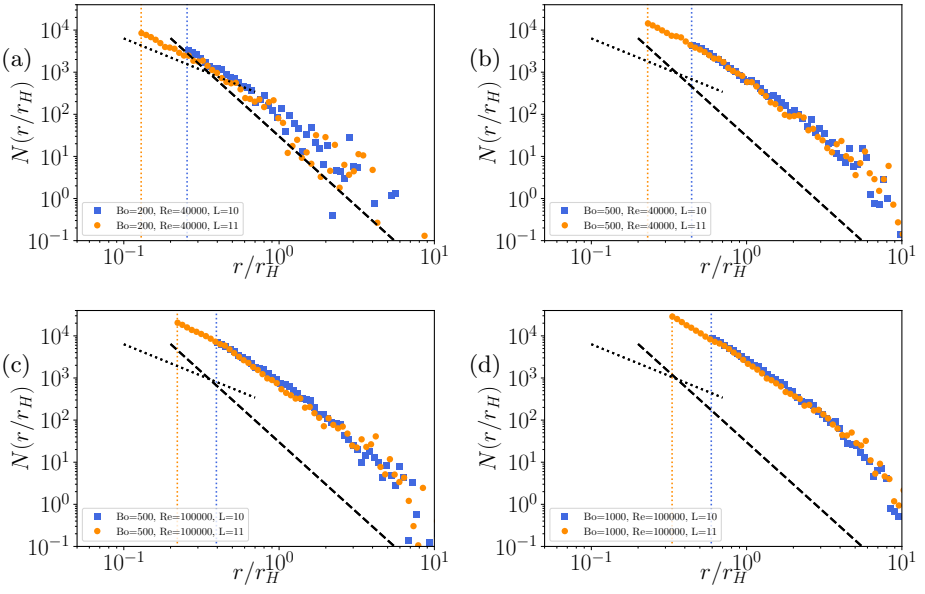

FIGURE 6. Bubble size distributions for the cases (a) Bo $= 200, \mathrm{Re} = 4 \times 10^4$; (b) Bo $= 500, \mathrm{Re} = 4 \times 10^4$, (c) Bo $= 500, \mathrm{Re} = 10^5$ (d) Bo $= 1000, \mathrm{Re} = 10^5$. Resolutions of comparison are $L = 10, 11$ where $\Delta x = 1/(2^L)$ is the minimum grid size. Data is time-averaged over $(t - t_{im})/T \in [0.4, 1.2]$. Vertical dotted lines (orange, blue) show the grid size (normalized by r_H; dashed line (black) shows $(r/r_H)^{-10/3}$; sloped dotted line (black) shows $(r/r_H)^{-3/2}$, based on fit by Deane & Stokes (2002).

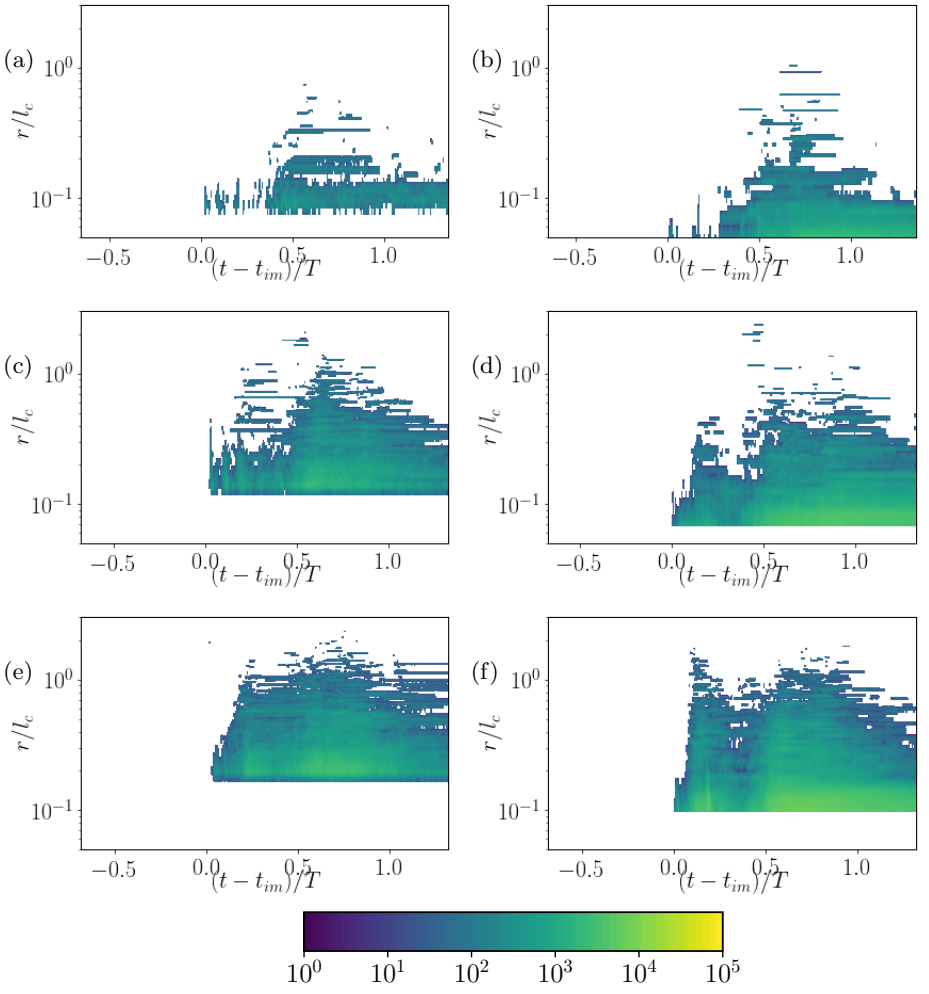

FIGURE 7. Droplet contour plots for different Bo, Re, and resolution. (a,b) $Bo = 200, Re = 4 \times 10^4$; (c,d) $Bo = 500, Re = 10^5$, (e,f) $Bo = 1000, Re = 10^5$. Resolutions are: (a,c,e) $L = 10$; (b,d,f) $L = 11$.

(8c) compares well between both resolutions, while the intermediate and late times are in good agreement for Bo $= 1000, \mathrm{Re} = 10^5$ (8d), for droplet sizes sufficiently larger than the mesh size.

Finally, figure 9 shows droplet size distributions for the cases $Bo = 200, Re = 4 \times 10^4$, $Bo = 500, Re = 4 \times 10^4$, $Bo = 500, Re = 10^5$, $Bo = 1000, Re = 10^5$, averaged over the times $(t - t_{im})/T \in [0.2, 1]$, for the resolution parameters $L = 10, 11$, corresponding with minimum grid sizes of $\Delta x = 1/(2^L)$. As before, the $Bo = 200$ case does not produce sufficient droplet populations to be considered statistically meaningful; the $Bo = 500$ and $Bo = 1000$ cases are approximately grid-converged for droplet radii greater than $\sim 2\Delta x$.

These observations suggest that: (i) Small Bond numbers less than 200 are not sufficient to produce numerically and statistically converged droplet statistics. (ii) Grid convergence is best obtained over time periods which extend to late in the

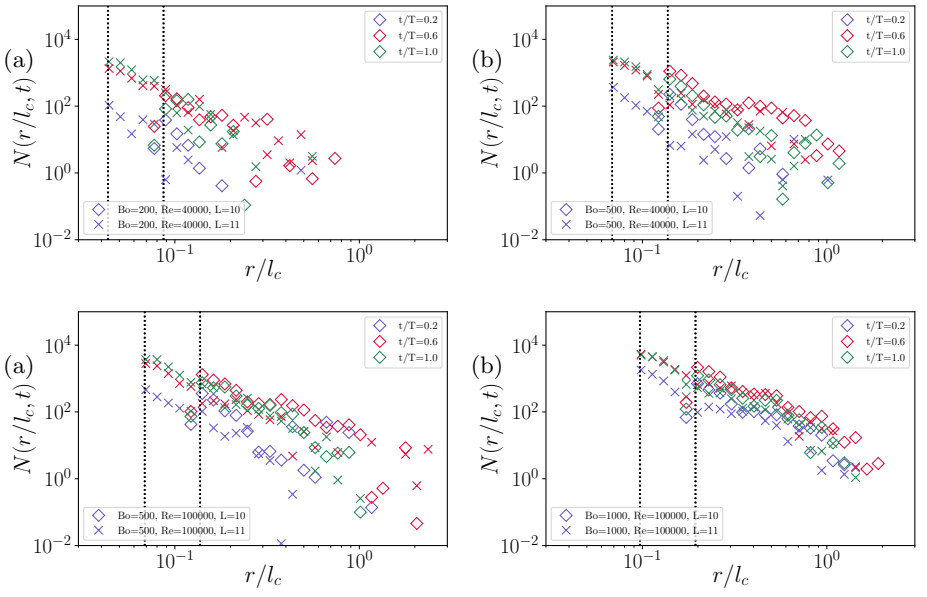

FIGURE 8. Numerical convergence of different time-averaging windows of droplet size distributions. Time-averaging windows are of width $\Delta t/T = 0.4$, and centered at $t/T = 0.2, 0.6, 1$, for cases (a) $\mathrm{Bo} = 200, \mathrm{Re} = 4 \times 10^4$, (b) $\mathrm{Bo} = 500, \mathrm{Re} = 4 \times 10^4$, (c) $\mathrm{Bo} = 500, \mathrm{Re} = 10^5$, (d) $\mathrm{Bo} = 1000, \mathrm{Re} = 10^5$.

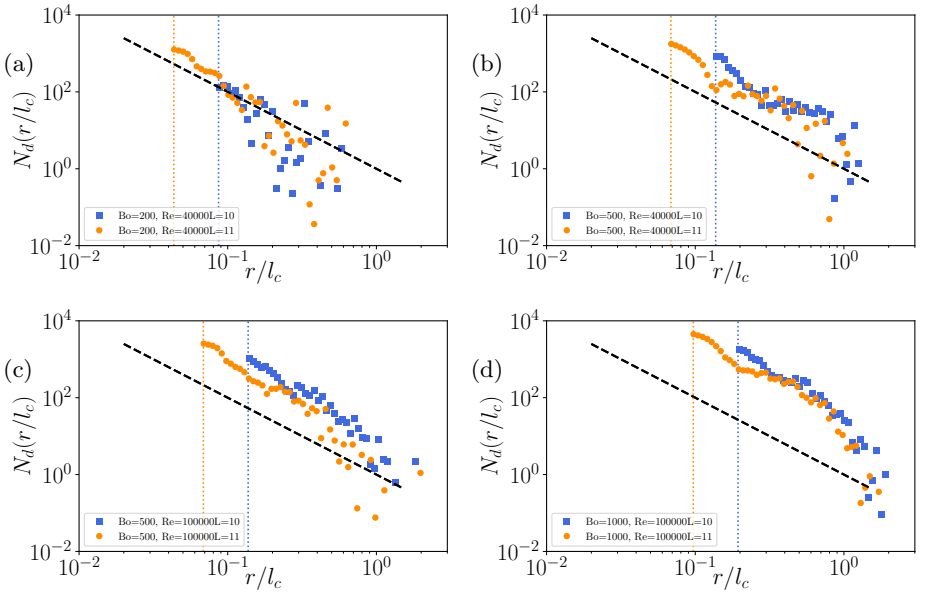

FIGURE 9. Droplet size distributions for the cases (a) $\mathrm{Bo} = 200, \mathrm{Re} = 4 \times 10^4$; (b) $\mathrm{Bo} = 500, \mathrm{Re} = 4 \times 10^4$; (c) $\mathrm{Bo} = 500, \mathrm{Re} = 10^5$; (d) $\mathrm{Bo} = 1000, \mathrm{Re} = 10^5$. Resolutions of comparison are $L = 10, 11$ where $\Delta x = 1/(2^L)$ is the minimum grid size. Data is time-averaged over $(t - t_{im})/T \in [0.2, 1]$. Vertical dotted lines (orange, blue) show the grid size (normalized by l_c); dashed line (black) shows $(r/r_H)^{-2}$, based on the fit by Erinin *et al.* (2019).

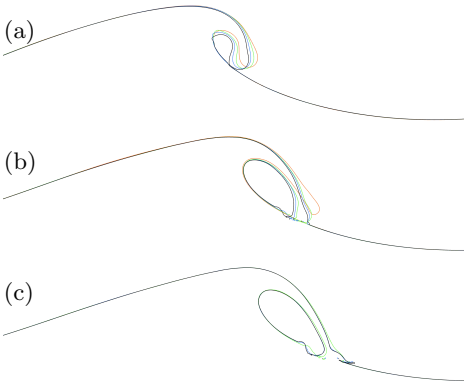

FIGURE 10. Wave shape near the moment of breaking, for (a) $\mathrm{Bo} = 200, \mathrm{Re} = 4 \times 10^4$, (b) $\mathrm{Bo} = 500, \mathrm{Re} = 10^5$, (c) $\mathrm{Bo} = 1000, \mathrm{Re} = 10^5$, at resolutions $L = 9$ (red), 10 (green), 11 (blue), 12 (black).

breaking process. This is attributed to the largest and most abundant droplets being produced during the later sustained splashing processes. (iii) In particular, the first spike at early times, corresponding with the secondary splash, comprises droplet populations that may not be fully grid-converged. This is consistent with this first spike not being fully distinct for lower-resolution cases in figure 7. (iv) Droplet size distributions are not numerically converged close to the mesh size at any resolution or Bond or Reynolds number, suggesting that at least 4-8 points are required per droplet diameter for numerical convergence. We note that ensemble averages would be useful to achieve statistical convergence and assess the resolution of the physical processes and their numerical convergence.

2.4. *Shape at impact*

Finally we consider the dependence of the wave shape close to breaker impact on maximum resolution level L. Figure 10 shows wave shapes for 2D breakers near the moment of impact. At low Bond and Reynolds numbers ($\mathrm{Bo} = 200, \mathrm{Re} = 4 \times 10^4$, figure 10a), the wave shape shows some variation with respect to resolution. But at higher Reynolds number and increasing Bond number (figures 10b,c), the breaker shape does not vary significantly with increasing resolution, and in figure 10c the agreement between shape between $L = 11, 12$ (blue, black) is excellent.

3. Mass conservation

Mass is well-conserved by the numerical method and the VOF reconstruction. Figure 11 shows the relative time variation in volume of the liquid and air phases in the case $\mathrm{Bo} = 500, \mathrm{Re} = 4 \times 10^4, L = 10$, which never exceeds 0.0001% (10^{-6}).

REFERENCES

De Vita, Francesco, Verzicco, Roberto & Iafrati, Alessandro 2018 Breaking of modulated wave groups: kinematics and energy dissipation processes. *Journal of fluid mechanics* **855**, 267–298.

Deane, Grant B & Stokes, M Dale 2002 Scale dependence of bubble creation mechanisms in breaking waves. *Nature* **418** (6900), 839–844.

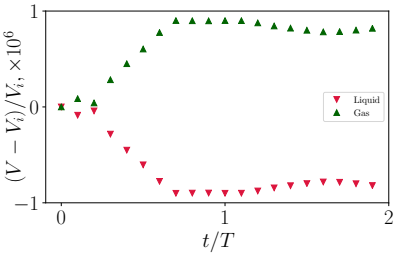

FIGURE 11. Relative variation of volume in the gas (green) and liquid (red) phases over time for the case $\mathrm{Bo} = 500, \mathrm{Re} = 4 \times 10^4, L = 10$.

DEIKE, L., POPINET, S. & MELVILLE, W.K. 2015 Capillary effects on wave breaking. *J. Fluid Mech.* **769**, 541569.

DODD, MICHAEL S, MOHADDES, DANYAL, FERRANTE, ANTONINO & IHME, MATTHIAS 2021 Analysis of droplet evaporation in isotropic turbulence through droplet-resolved dns. *International Journal of Heat and Mass Transfer* **172**, 121157.

ERININ, MARTIN A, WANG, SOPHIE D, LIU, REN, TOWLE, DAVID, LIU, XINAN & DUNCAN, JAMES H 2019 Spray generation by a plunging breaker. *Geophysical Research Letters* **46** (14), 8244–8251.

FUSTER, DANIEL & POPINET, STÉPHANE 2018 An all-mach method for the simulation of bubble dynamics problems in the presence of surface tension. *Journal of Computational Physics* **374**, 752–768.

VAN HOOFT, J ANTOON, POPINET, STÉPHANE, VAN HEERWAARDEN, CHIEL C, VAN DER LINDEN, STEVEN JA, DE ROODE, STEPHAN R & VAN DE WIEL, BAS JH 2018 Towards adaptive grids for atmospheric boundary-layer simulations. *Boundary-layer meteorology* **167** (3), 421–443.

POPE, S.B. 2000 *Turbulent flows*. Cambridge University Press.

POPINET, S. 2003 Gerris: a tree-based adaptive solver for the incompressible euler equations in complex geometries. *J. Comput. Phys.* **190** (2), 572 – 600.

POPINET, S. 2009 An accurate adaptive solver for surface-tension-driven interfacial flows. *J. Comput. Phys.* **228** (16), 5838 – 5866.

POPINET, STÉPHANE 2018 Numerical models of surface tension. *Annual Review of Fluid Mechanics* **50**.